Different principles govern different scales of brain folding

Arka N. Mallela M.D.[1]; Hansen Deng, MD[1]; Alan Bush PhD.[2]; Ezequiel Goldschmidt M.D., Ph.D.[1]

1. Department of Neurosurgery, University of Pittsburgh Medical Center, Pittsburgh, Pennsylvania, United States of America
2. Department of Neurosurgery, Massachusetts General Hospital, Boston, Massachusetts, United States of America

*Corresponding author
Ezequiel Goldschmidt, M.D., Ph.D.
AANS Van Wagenen Fellow
Department of Neurological Surgery
University of Pittsburgh Medical Center
UPMC Presbyterian Hospital
200 Lothrop Street, Suite B-400
Pittsburgh, PA 15213
E-mail: goldschmidted@upmc.edu
Phone: 412-647-6777
Fax: 412-647-6483

Key words: brain folding; gyrification; fetal MRI; Sylvian Fissure, nonlinear registration

Funding Statement
This research received no specific grant from any funding agency in the public, commercial or not-for-profit sectors.

Competing Interests Statement
The authors have no personal or institutional interest with regards to the authorship and/or publication of this manuscript.

Contributions Statement
EG, AB and AM were involved in the design and conception of this manuscript. EG, HD and AM performed the literature search. EG, AB, HD and AM compiled the primary manuscript. EG and AM compiled the figures. EG, AM, HD and AB critically revised the manuscript. All authors have approved the manuscript as it is written.

ABSTRACT

The signature folds of the human brain are formed through a complex and developmentally regulated process. *In vitro* and *in silico* models of this process demonstrate a random pattern of sulci and gyri, unlike the highly ordered and conserved structure seen in the human cortex. Here, we account for the large-scale pattern of cortical folding by combining advanced fetal MRI with nonlinear diffeomorphic registration and volumetric analysis. Our analysis demonstrates that *in utero* brain growth follows a logistic curve, in the absence of a lack of external volume constraints. The Sylvian fissure forms from interlobar folding, where separate lobes overgrow and close an existing subarachnoid space. In contrast, other large sulci, which are the ones represented in existing models, fold through an invagination of a flat surface, a mechanistically different process. Analyzing local variations in volumetric expansion rates, we demonstrate that the three phases of the logistic curve correspond to three different phases of folding - interlobar, large sulcal, and secondary folding. Cortical folding is driven by multiple spatially and temporally different mechanisms, therefore regionally distinct biological process may be responsible for the global geometry of the adult brain.

64 **SIGNIFICANCE**

65 Understanding brain folding is key to recognizing the functional differentiation of the brain and how
66 neurodevelopmental disorders disrupt this process. Previous reports have modeled this process in animal models,
67 *in vitro*, and *in silico*. Nevertheless, we do not have a thorough understanding of normal human fetal brain folding
68 during gestation. Here, we use *in utero* fetal MRI to demonstrate three spatiotemporally distinct phases of folding.

69

70 **INTRODUCTION**

71 Mechanisms underlying gyrification of the human cerebral cortex have been investigated for decades.
72 Folding is a dynamic and complex process driven by tangential cortical expansion(1, 2) and differential cell growth
73 in and around the subventricular zone (SVZ) (3–7). Mechanisms such as a volume constraint from the skull (3, 8)
74 and tension forces from axons (9, 10) have not received further validation. Tallinen et al. simulated the triple
75 junction folding of the mammalian cortex using a soft elastic bilayers with variable growth rates *in silico*(11, 12).
76 The model introduced in this landmark paper produced folds resembling cortical gyri morphologically but did not
77 explain the highly conserved spacing and orientation of gyri. To account for the biology of a preserved cortical
78 pattern, multiple reports have studied folding in ferrets (5, 10). This is an ideal model to understand the formation
79 of individual gyri and the differences between sulcal and gyral molecular signatures but does not explain the global
80 geometry of the mature telencephalon.

81 To further guide these models and understand the global pattern of gyrification, analysis of human cortical
82 folding *in vivo* is required. Hill et al. studied postnatal human and macaque brain folding, illustrating that patterned
83 differential expansion in cortex drives an orderly progression of postnatal brain folding(13), Garcia et al. studied
84 pre-term and post-natal magnetic resonance imaging (MRI) scans and identified regional differences of cortical
85 growth beginning at an estimated gestational age (GA) of 28 weeks. Notably, increased growth was first observed
86 near the central sulcus from GA 28-30, and subsequently progressing outwards to the frontal and temporal
87 poles(14). Finally, Rajagopalan et al. utilized *in utero* MRI in a cohort of 40 individuals from GA 20-28 and found

88 similar areas of differential expansion driving cortical folding(15). Here, we build on these analyses by using the
89 latest advancements in fetal MRI reconstruction, fetal atlas construction, and nonlinear diffeomorphic
90 registration.

91 We hypothesize that cortical folding is driven by multiple spatially and temporally distinct processes. To
92 demonstrate this, we utilized a fetal brain MRI atlas constructed from 81 individuals(16) to study changes in the
93 cortical topography in relation to the subarachnoid space at various points of pre-natal maturation, from GA 21
94 to 38. Our analyses show that interlobar folding, formation of large (named) sulci, and formation of secondary
95 (nonnamed) sulci are morphologically different. Moreover, these proceed in an orderly fashion during
96 development. These findings support the hypothesis that different scales of brain folding are driven by different
97 mechanisms, small and large scale gyrification may obey distinct principles.

98

99

100 **RESULTS**

101

102 **Intracranial expansion by compartment**

103 We segmented each week into various compartments - intracranial volume, total cerebral volume,
104 subarachnoid space, and lateral ventricles. We further divided the subarachnoid space into the subdural
105 subarachnoid space – the space between the lateral border of the cerebrum and dura, reflecting the space
106 between brain and dura, and the sulcal subarachnoid space – the space contained within the sulci/fissures of the
107 brain (**Figure 1A**).

108 From GA 21 to GA 38 the total volume of the cerebrum increased nearly 6-fold from 50 cm^3 at GA 21 to
109 279 cm^3 at GA 38. Congruently, the total subarachnoid space increased 4-fold from 32 cm^3 at GA 21 to 120 cm^3 at
110 GA 38. The ventricles, on the other hand, represented a small volume of 3 cm^3 at GA 21 grew only 2-fold to 6 cm^3
111 throughout gestation. We observed maximum intracranial expansion between weeks 25 and 34. (**Figure 1B)**.

We found that a logistic growth model best fits the cerebral volume over gestation **(Figure 1C)**. This parcellates growth into 3 phases. From Week 21 to 25 growth is relatively slow, but the growth rate increases between week 25 and 34, with a final tapering. The model predicts a final (term) volume of 330 cm^3 and a maximum weekly growth rate of 17 cm^3 per week at approximately 28 weeks.

In relative terms, cerebral volume expands from 56% to 63% of intracranial volume. While total subarachnoid relative volume decreases from 36% to 27%, this is largely driven by loss in subdural subarachnoid space (25% to 15%). Importantly, almost a third of the intracranial volume corresponds to subdural space at the end of gestation. Thus, cortical folding of the brain occurs in the presence of abundant subdural subarachnoid space and a lack of an external volume constraint. Interestingly the sulcal subarachnoid relative volume remains essentially constant from 11% to 12%, suggesting that globally the folding process creates and obliterates equal relative amounts of subarachnoid space. (**Figure 1D).**

The Sylvian fissure folds differently than other sulci

The majority of cerebral sulci are elongated depressions between two raised gyri. This type of folding occurs in parallel with intracranial expansion and is the most prevalent type of sulcal formation. As the bordering gyri increase in volume, the sulcus deepens, and both should show a correlated increase in total volume. To analyze this form of folding, we segmented each sulcus/fissure and identified the surrounding gyri.

We used the left parieto-occipital and calcarine sulci to characterize this form of folding. In these sulci, both the volumes of the sulcal edges and the sulcal subarachnoid space increased with time, which resulted in a direct correlation ($r = 0.99$ and $r = 0.95$, respectively; **Figure 2 center, right**).

The Sylvian fissure, on the other hand, appears to form from a flat depression that is closed through the convergence of two edges. It first appears on the lateral aspect of the cerebral hemisphere before other folds are present. Subsequently, there is a gradual confluence of the anterior and posterior edges of the depression which closes the depression. These edges develop into the frontal and temporal opercula and the depression itself forms

136 the insula (**Figure 3**). This mechanism of folding is completely different than that of other sulci and fissures,
137 exemplified here by the parietooccipital and calcarine fissures. The growth of these Sylvian opercula is inversely
138 correlated with the growth of the Sylvian subarachnoid space (r = -0.97; **Figure 2, left**). The Sylvian fissure forms
139 through a convergent closure as opposed to the invagination characteristic of other sulci – as the bordering gyri
140 grow, the Sylvian fissure shrinks.
141
142 **Spatiotemporally distinct processes fold the brain at multiple scales**
143 Relative volumetric change (as determined by the Jacobian determinant) were quantified in both the left
144 and right hemispheres and are rendered in **Figure 4**. Phase 1 (top) is "interlobar folding". The second phase
145 (middle) is the formation of large, named, sulci. Finally, Phase 3 is the formation of small secondary sulci and focal
146 areas of growth. As described in the methods, the Jacobian is corrected for *global* volume growth, so local loss in
147 volume still may represent overall growth.
148
149 *Lateral hemispheric surface*
150 In phase 1, the primary area of folding is the frontal, parietal, and temporal opercula, with closure of the
151 Sylvian fissure. From GA 23 to 25, the depression that becomes the future insula becomes closed off in the
152 posterior aspect, and the gross morphology of the major lobes is formed. Volumetric change was first observed
153 at the supramarginal gyrus starting in GA 23, then moved anteriorly to the frontal lobe and laterally in the direction
154 of the temporal pole. This "C" shaped expansion originates from the area that will become the supramarginal
155 gyrus eventually reaching the future pre-central gyrus. From GA 25 to 31, focal volume growth was observed
156 around the forming Sylvian fissure and the incipient central sulcus. In the frontal and parietal lobes, the central
157 sulcus forms first and then sulcation proceeds in an orderly fashion outward from the central sulcus. The central
158 sulcus is apparent by GA 26, the pre and post central sulci by GA 28-29, the intraparietal sulcus by GA 29, and the
159 superior and inferior frontal sulci by GA 31. In the temporal lobe, the superior temporal sulcus appears to form

first, by approximately GA 29 and then inferior temporal sulcus appears to be forming at GA 31. By the beginning of phase 3 at GA 32, the major sulci of the brain have formed and are clearly recognizable. However, folding continues to proceed with the formation of additional convolutions. Unlike previous phases, there does not appear to be an orderly progression of folding, with only the temporal pole and frontal operculum appearing to have consistent volume expansion.

Medial hemispheric surface

Spatiotemporal mapping of the medial hemispheres revealed that the cingulum underwent the greatest differential volumetric change. By GA 24, a yet unfolded brain exhibited increased growth in 3 regions involving the medial frontal lobe, the center of the cingulum, and the occipital lobe in what will become the anatomical parieto-occipital sulcus. By week 26, at the beginning of Phase 2, these high-growth areas formed an inverted "U," marked posteriorly by a low-growth area in the precuneus. Similar to development observed on the lateral bi-hemispheric surfaces, there was volumetric expansion of the paracentral lobule (the representation of the pre and post central gyri on the medial surface) slowing by week 31-33. By Week 29, a clear parieto-occipital sulcus is visible. Interestingly volumetric growth around the cingulate sulcus is the norm for most of Phase 2, only slowing near the end. In phase 3, expansion is constrained to a few dispersed areas, without a clear pattern in folding, similar to the growth on the lateral hemisphere.

Ventricular zone

Figure 4 demonstrates significant growth at the cortical surface. Interestingly, while the subplate zone also demonstrates volumetric expansion, the ventricular zone (VZ) does not (**Figure S1**). There is a clear boundary running through the SVZ dividing this area of relative expansion vs. relative contraction in the VZ. This dichotomy between superficial and deep structure persists across all GA in this study.

Validation of registration

In order to validate our registration method, we compared three registration/warp paradigms – Week 38 to 21 (with intensity information only), Week 21 to 38 (with intensity information only), and Week 38 to 21 with landmarks. We warped segmentations week-to-week (**Table S1**) and cumulative across all weeks starting from either Week 21 or 38 (first/last weeks) (**Table S2**) and compared them to the preexisting segmentation using the weighted multiclass Dice similarity coefficient (range: 0 – no overlap, to 1 – perfect overlap).

For the registration used for our final experiments (Week 38 to 21), the week-to-week comparison Dice coefficient ranged from 0.89 to 0.94 (**Table S1**), while the cumulative comparison – warping the Week 38 segmentation across all weeks – ranged from 0.9 (week 38 to 37) to 0.72 (week 38 warped via concatenated transformations to week 21) (**Table S2**).

Overlap when segmentations were warped in the forward direction, from week 21 to 38, were comparable in the week-to-week comparison, ranging from 0.89 to 0.94 (**Table S1**). However, in the cumulative comparison, this paradigm fared slightly worse, with Dice coefficients ranging from 0.9 (week 21 to 22) to 0.68 (week 21 warped via concatenated transformations), reflecting greater accumulated registration error in this paradigm (**Table S2**).

Interestingly, when the registration algorithm was given the preexisting segmentation as a landmark in addition to image intensity, overlap worsened both in week-to week (0.87 – 0.91, **Table S1**) and cumulative comparisons (0.9 to 0.56, **Table S2**).

DISCUSSION

In the second and third trimesters of gestation, the cerebrum undergoes regulated expansion and the formation of gyri and sulci. Previous investigations have proposed multiple mechanisms for the folding of a smooth cortical plate into a highly convoluted cortex (3–5, 9, 11, 12, 14, 17–21). Most of these models have

208 rendered a prototypical sulcus, but few have studied the development of the entire human cortex *in vivo* (13–15,
209 22). None have systematically mapped the spatiotemporal folding of the cortex in the second and third trimesters.
210 Our present study does so, specifically highlighting on a week-to-week basis how distinct spatiotemporal
211 processes gyrify the brain *in utero*.

212 We elected to analyze the Gholipour atlas (16) as it was the highest resolution available dataset and
213 provided much higher signal-to-noise ratio than an individual fetal MRI. Given that this atlas was constructed as a
214 normative group mean of 81 fetuses, we expect that our findings will translate to the individual setting.

215

216 **Cerebral growth is internally constrained.**

217 Our study demonstrated that both the intra-axial and extra-axial spaces grow significantly during
218 gestation (**Figure 1**). At birth, more than 15% of the total intracranial volume corresponds to subdural
219 subarachnoid space, indicating a significant layer of CSF between the cerebrum and inner table of the skull. This
220 further strongly suggests that cortical folding of the brain is not driven by a mechanical extra-axial constraint.
221 Moreover, there is increasing proteomic evidence that the CSF provides a proliferative niche during embryonic
222 development via fibroblast growth factor(23) and insulin-like growth factor(24), among other signaling molecules.

223 Yet, our analysis indicates that cerebral growth still slows by late gestation, following a logistic curve, with
224 a term volume of 330 cm^3, similar to previous reports in the literature(25). Similarly, Dubois et al. found that
225 perinatal brain growth follows a Gompertzian curve, an asymmetric relative of the logistic curve (26). Both models
226 indicate a constraint to unrestrained growth – such as cell-to-cell signaling, internal mechanical constraints,
227 among other mechanisms(27, 28). Despite a lack of an *external* volumetric constraint, other internal phenomena
228 alter and shape the growth of the cerebrum.

229

230

231

232 **Different principles govern different scales of brain folding**

233 The development of the Sylvian fissure, the exemplar of interlobar folding and the main depression
234 responsible for the global configuration of the mature brain, is a fundamentally different process than large sulci
235 formation. Morphologically, the Sylvian fissure *closes* while the major other sulci *deepen*. This is apparent both
236 qualitatively from the maps of volume expansion (**Figure 4 – Phase 1 and 2**) and quantitatively (**Figure 2**). The
237 borders of the calcarine and parietoocipital sulci expand outwards while the sulci deepen – both expand in volume
238 in a correlated fashion. In contrast, as the opercular gyri grow, the Sylvian fissure shrinks – in an anticorrelated
239 fashion (**Figures 2 and 3**). This suggests that different biophysical, genetic, and cellular growth mechanisms fold
240 the Sylvian fissure.

241 The presence of a distinct mechanism for interlobar folding is supported by two observations. First, global
242 malformations of cortical development can have sulci without the Sylvian fissure or vice versa. For example, in
243 alobar holoprosencephaly, sulci can be present, but there is no global structure to the brain, let alone a Sylvian
244 fissure. In contrast, in lissencephaly, there is a Sylvian fissure but few to no other sulci. Finally, even in
245 polymicrogyria, often a Sylvian fissure is present even though all other sulci are malformed(29). This suggests that
246 the mechanisms for interlobar folding and sulcation are different. Second, recent work by Bush et al. (30), seeks
247 to explain why no middle cerebral artery branches cross the Sylvian fissure, when *every other sulcus* has traversing
248 arteries. The authors developed a novel convergence index calculated as the ratio of shortest cortical path to
249 physical distance. Using this they demonstrate that the frontal and temporal opercula have the highest degree of
250 convergence of any cortical structure, implying that they begin in fetal life distant from one another and the
251 converge over time. In contrast, the borders of other sulci do not converge to such a high degree. This again
252 suggests that interlobar folding and large sulcation are distinct processes.

253 Following interlobar folding, the brain appears to undergo an orderly progression of folding during large
254 sulcation, beginning with the formation of the central sulcus and superior temporal sulcus, and progressing
255 outwards/inferiorly. This is driven by regions of higher expansion compared to the surrounding cortex. Garcia et

al. described such regions of high growth being located around the insula and migrating outward from the central sulcus (31). Likewise, both Rajagopalan et al. (15) and Dubois et al. (26) found a similar ordered pattern of folding during the late second and early third trimesters, while Garcia et al. demonstrated this outward progression from the central sulcus in preterm but postnatal babies. Interestingly, they analyzed changes in curvature or spatial frequencies of gyri, instead of volumetric changes analyzed here. All three approaches reached similar conclusions despite different methods of analysis, lending further credence to this hypothesis. A purely mechanical explanation cannot account for the highly conserved and ordered nature of this process.

In contrast, the formation of secondary non-named sulci, such as branches off the superior/inferior frontal sulci and the variable branching of the intraparietal sulcus form later in neurodevelopment, following GA week 32. Unlike in the previous two phases, we did not observe discrete areas of consistent relative volumetric expansion (**Figure 4 – Phase 3**). These sulci are less conserved than the large sulci, exhibiting greater variability between individuals(32, 33). This form of folding may be the result of tangential expansion and mechanical creasing, as proposed by Tallinen et al. (11, 12, 20). Thus, we find that patterns of large-scale folding are qualitatively different from that of secondary sulcation.

Our analysis suggests that the 3 phases of the logistic curve correspond closely to the three phases of folding – interlobar folding (exemplified by the formation of the Sylvian fissure) until approximately GA 25 weeks (**Figure 4 – Phase 1**), large sulcation (e.g. the central sulcus, pre/post central sulci, temporal sulci) from GA 26 to 31 weeks (**Figure 4 – Phase 2**), and secondary sulcation (**Figure 4 – Phase 3**), from 32 weeks to term. Others have reported a similar periodization, although nomenclature varies, particularly as to what constitutes primary and secondary sulcation. (15, 34–37).

Asymmetries and divisions in growth

We additionally noted a left/right asymmetry in our Jacobian analysis. A left-right asymmetry was first noticed by direct observation of 507 fetal brains by Chi et al., who noticed that the superior frontal and temporal

280 gyri appeared one or two weeks before on the right side (34). These findings were later confirmed by Leroy et al.,
281 who also described lateral asymmetries specific to humans and that persist during and after gestation(38). This
282 may speak to the genetic nature of the folding process.

283 Finally, we note that majority of volumetric expansion occurs in the cortex and subplate, with
284 comparatively little to no expansion occurring in the ventricular zone from GA weeks 21 to 38 (**Figure S1**). There
285 appears to be a boundary running through the subventricular zone that divides areas of relative expansion and
286 lack of expansion. Our atlas does not delineate the SVZ exactly or the boundary between the outer and inner SVZ,
287 so we are unable to assess exactly whether our boundary corresponds to a cellular boundary. Nevertheless, this
288 line dividing areas of expansion and lack of expansion is consistent with both a mechanical bilayer tangential
289 growth explanation and an outer SVZ cell growth model but is less consistent with axonal tension models.

290

291

292 **Underlying patterning is required to explain phases of folding.**

293 A purely mechanical explanation is insufficient to explain our and others' findings regarding interlobar
294 folding and large sulcation but may explain secondary sulcation. Findings from other developmental studies
295 suggest that this may be driven by underlying genetic or proteomic patterning in the ventricular zone in the first
296 and second trimesters(5, 39–42). Nonuniform expression of transcription or growth factors in the ventricular zone
297 may unlock greater growth at a later phase of development, once intermediate progenitor cells have migrated to
298 the subventricular zone. Cells found in of high growth in the Jacobian analysis may have unique expression profiles
299 and are prime targets for tissue analysis.

300 Mechanical phenomena can explain *how* sulci form, but not where and when they form. Further, less
301 conserved secondary folding may be a purely mechanical phenomenon.

302

303

CONCLUSIONS

Brain folding is not a homogenous process and different principles are required to explain the different phases of folding. Using *in utero* fetal MRI, we demonstrate that interlobar folding, large sulcation, and secondary sulcation are morphologically different. A purely mechanical explanation cannot explain the highly patterned nature of these processes.

309 **METHODS**

310

311 **Fetal brain MRI**

312 We utilized a digital fetal brain atlas constructed from 81 healthy fetuses, spanning GA 21 to 38, developed
313 by Gholipour et al. (16). Full acquisition details are described in that report. The full content of the atlas can be
314 accessed at http://crl.med.harvard.edu/research/fetal_brain_atlas/.

315 In brief, the authors acquired structural images using repeated T2-weighted half-Fourier acquisition single
316 shot fast spine echo (T2wSSFSE) series over an acquisition period of 15 to 30 minutes on 3T Siemens Skyra or Trio
317 MRI scanners (Siemens Healthineers, Erlangen, Germany). Images were preprocessed with motion and bias field
318 correction and super-resolution volumetric reconstruction. The atlas was then constructed from volumetric
319 reconstructions utilizing kernel regression over time and symmetric diffeomorphic deformable registration in
320 space. Fetal atlas segmentation of cortical and deep structures was initialized using a previous segmentation
321 developed by Gousias et al.(43, 44) and propagated to all gestational ages.

322

323 **Registration and validation**

324 To identify and quantify week-to-week brain development, we utilized the Symmetric Normalization (SyN)
325 algorithm in the Advanced Normalization Tools (*ANTs*) package to register weekly image pairs (Week 21 to 22, 22
326 to 23, etc.). This algorithm, a form of symmetric diffeomorphic nonlinear registration, can identify large
327 deformations in tissue morphology while ensuring invertibility, smoothness, and preserving topology (i.e gyri do
328 not intersect one another, brain curvature does not reach an unphysically high value). These registrations are
329 mathematically invertible, allowing for studying week-to-week changes both in the forward and backward
330 directions(45–48).

331 We studied three registration/warping paradigms. For the first two, the registration metric only used
332 image intensity (mutual information) and no additional segmentation or landmark data (that might influence

growth predictions). The first registered and warped segmentations from Week 38 to 37, 37 to 36, etc. ("Week 38 to 21"), while the second registered from Week 21 to 22, 22 to 23, etc. ("Week 21 to 38"). For a third method we used both image mutual information and landmark (segmentation) overlap as registration metrics, and registered from Week 38 to 37, 37 to 36 etc. ("Week 38 to 21 with landmarks")

We used the preexisting segmentations in the Gholipour et al. atlas (49) as the ground truth to validate the accuracy of our registration. For the first validation, we warped each preexisting segmentation by 1 week (Week 38 to 37, etc.). For the second, we warped the initial segmentation (Week 38 for the Week 38 to 21 and Week 38 to 21 with landmarks paradigms, Week 21 for the Week 21 to 38 paradigm) through all weeks. We then compared the overlap of the warped segmentations to the preexisting segmentations. using the weighted multiclass Dice similarity coefficient (DSC). The DSC ranges from 0 (no overlap) to 1 (perfect overlap).

As described in the results, the Week 38 to 21 registration paradigm was superior and was used for the remainder of the study. Notably, the only matching criteria used for our final registration was image intensity. No *a priori* segmentation or landmarks were used in our final registration, allowing the algorithm to identify tissue correspondences without outside guidance. Interestingly, when pre-existing segmentations were provided to the registration algorithm, registration accuracy actually worsened (**Tables S1/S2**), suggesting that our registration algorithm may identify correspondences between weeks that do not correspond to conventional boundaries between gyri, sulci, and subcortical structures. We utilized the *ANTsPy* python wrapper around the *ANTs* package and the *Scikit-learn* package in Python(50).

Segmentation

While the original atlas contained several key structures, others, including notable subarachnoid cisterns and sulci, were not included. As such, we algorithmically generated segmentations of the posterior fossa, Sylvian fissure, calcarine sulcus, parietoocipital sulcus and falx cerebri by using the procedure described by Glaister et al. (51). In essence this method identifies all cerebrospinal fluid (CSF) voxels lying between predefined cerebral

357 structures. The posterior fossa space was defined using segmentations of the cerebellum, medulla, pons and
358 midbrain, as well as the associated CSF space. The Sylvian fissure was defined as the CSF space lying between the
359 margins of the frontal operculum, temporal operculum, and supramarginal gyrus. The calcarine sulcus was defined
360 as the sulcus between the cuneus and lingual gyri, and the parietoocipital sulcus as the sulcus between the
361 precuneus and cuneus.

362 Intracranial volume was defined as all intradural volume. The intracranial space was differentiated into
363 the volumes of the cerebrum, ventricles, and the subarachnoid space. The cerebral volume was defined as the
364 total brain volume lying above the tentorium cerebelli. The brainstem and its associated cisterns were excluded
365 from the analysis since they are not part of the cortical folding process. The ventricles were defined using the
366 preexisting segmentation (16). The subarachnoid space was defined as all supratentorial CSF space. This space
367 was further subdivided. The sulcal subarachnoid space was defined as space contained within the sulci/fissures of
368 the brain and which would be directly affected by gyration/sulcation. In contrast, the subdural subarachnoid
369 space, that is, the overlying space between the lateral border of the cerebrum and the dura, reflects how close
370 the brain gets to the skull during development. This was done by constructing a convex hull for each cerebral
371 hemisphere at each gestational point during fetal development. CSF voxels within the shell were termed the sulcal
372 subarachnoid whereas space outside of the shell was subdural subarachnoid (**Figure 1A**)

373

374 **Volumetric Analysis**

375 We calculated the volumes of total intracranial compartments (intracranial, cerebral, subarachnoid, etc.)
376 and for each analyzed sulcus (Sylvian fissure, parietoocipital sulcus, calcarine sulcus) and the surrounding cortical
377 structures. For global volumetric analysis, we analyzed changes in intracranial compartment volume overtime and
378 performed nonlinear regressions to identify a candidate model for cerebral volume growth. For sulcal volumetric
379 analysis, we calculated the volume of each sulcus and surrounding cortical structures. We analyzed the
380 relationship between sulcus volume and surrounding gyri volumes for each sulci studied.

Neuroimaging data analysis was performed utilizing the *NumPy* and *NiBabel* packages in Python (Python 3.5). Statistical analysis was conducted using the *pandas* package and data plots were generated using *matplotlib* (Matplotlib version 3.1.1) in Python(52).

Jacobian Analysis

To map local volumetric changes, the Jacobian determinant was computed at each point for each transformation. The Jacobian determinant quantifies local volumetric change at a given point, with values greater than 1 representing expansion and those less then 1 representing compression. The ANTS algorithm calculates a separate affine transformation and a nonlinear transformation for each registration. The affine transformation accounts for global scaling, transformation, rotation, etc. while the nonlinear component identifies local changes. Here, the Jacobian determinant is calculated from the nonlinear component only. As such, the Jacobian determinant values here is corrected for global volume expansion (scaling). For example, if the registration identified a 10% global expansion, a Jacobian determinant value of 1.1 (+ 10%) represents a total expansion of 20% while a a value of 0.91 (-9%) represents a total expansion of 1%. This was calculated utilizing the *ANTs* toolbox.

Visualization

We generated 3D surface visualizations to facilitate intuitive understanding of our findings. For figures illustrating sulci and surrounding gyri, we utilized 3D rendering in *itk-snap* (53). To illustrate the cortical variation in the Jacobian determinant, we computed a 3D mesh of the cortical surface at each GA using the marching cubes algorithm in the *scikit-image* package and smoothed our mesh using *trimesh*. Jacobian determinant maps were overlaid on this mesh using *nilearn*.

All packages were run on Python 3.7 and utilized under the BSD or GNU license allowing for use in scientific settings.

Acknowledgements

We thank the authors of Gholipour et al. (16) for making their fetal atlas database publicly available to the scientific community and supporting work such as this.

References

1. P. V. Bayly, L. A. Taber, C. D. Kroenke, Mechanical forces in cerebral cortical folding: A review of measurements and models. *J. Mech. Behav. Biomed. Mater.* **29**, 568–581 (2014).
2. C. D. Kroenke, P. V. Bayly, How forces fold the cerebral cortex. *J. Neurosci.* **38**, 767–775 (2018).
3. V. Fernández, C. Llinares-Benadero, V. Borrell, Cerebral cortex expansion and folding: what have we learned? *EMBO J.* **35**, 1021–1044 (2016).
4. V. Borrell, How cells fold the cerebral cortex. *J. Neurosci.* **38**, 776–783 (2018).
5. I. Reillo, C. de Juan Romero, M. Á. García-Cabezas, V. Borrell, A role for intermediate radial glia in the tangential expansion of the mammalian cerebral cortex. *Cereb. Cortex* **21**, 1674–94 (2011).
6. S. Aydin, S. Yilmazlar, S. Aker, E. Korfali, Anatomy of the floor of the third ventricle in relation to endoscopic ventriculostomy. *Clin Anat* **22**, 916–924 (2009).
7. J. H. Lui, D. V. Hansen, A. R. Kriegstein, Development and evolution of the human neocortex. *Cell* **146**, 18–36 (2011).
8. W. Welker, “Why Does Cerebral Cortex Fissure and Fold?” in (1990), pp. 3–136.
9. E. Van D.C., A tension-based theory of morphogenesis and compact wiring in the central nervous system. *Nature* **385**, 313–318 (1997).
10. G. Xu, *et al.*, Axons pull on the brain, but tension does not drive cortical folding. *J. Biomech. Eng.* **132** (2010).
11. T. Tallinen, *et al.*, On the growth and form of cortical convolutions. *Nat. Phys.* **12**, 588–593 (2016).
12. T. Tallinen, J. Y. Chung, J. S. Biggins, L. Mahadevan, Gyrification from constrained cortical expansion. *Proc. Natl. Acad. Sci. U. S. A.* **111**, 12667–12672 (2014).
13. J. Hill, *et al.*, Similar patterns of cortical expansion during human development and evolution. *Proc. Natl. Acad. Sci. U. S. A.* **107**, 13135–13140 (2010).
14. K. E. Garcia, C. D. Kroenke, P. V. Bayly, Mechanics of cortical folding: Stress, growth and stability. *Philos. Trans. R. Soc. B Biol. Sci.* **373** (2018).
15. V. Rajagopalan, *et al.*, Local tissue growth patterns underlying normal fetal human brain gyrification quantified in utero. *J. Neurosci.* **31**, 2878–2887 (2011).
16. A. Gholipour, *et al.*, A normative spatiotemporal MRI atlas of the fetal brain for automatic segmentation and analysis of early brain growth. *Sci. Rep.* **7**, 476 (2017).
17. C. C. Hilgetag, H. Barbas, Role of mechanical factors in the morphology of the primate cerebral cortex. *PLoS Comput. Biol.* **2**, 146–159 (2006).
18. J. Dubois, *et al.*, The early development of brain white matter: A review of imaging studies in fetuses, newborns and infants. *Neuroscience* **276**, 48–71 (2014).
19. K. Zilles, N. Palomero-Gallagher, K. Amunts, Development of cortical folding during evolution and ontogeny. *Trends Neurosci.* **36**, 275–284 (2013).
20. T. Tallinen, J. S. Biggins, Mechanics of invagination and folding: Hybridized instabilities when one soft tissue grows on another. *Phys. Rev. E - Stat. Nonlinear, Soft Matter Phys.* **92** (2015).
21. S. Herculano-Houzel, B. Mota, P. Wong, J. H. Kaas, Connectivity-driven white matter scaling and folding in primate cerebral cortex. *Proc. Natl. Acad. Sci. U. S. A.* **107**, 19008–19013 (2010).
22. V. Rajagopalan, *et al.*, Mapping directionality specific volume changes using tensor based morphometry: an application to the study of gyrogenesis and lateralization of the human fetal brain. *Neuroimage* **63**, 947–58 (2012).
23. C. Martín, *et al.*, FGF2 plays a key role in embryonic cerebrospinal fluid trophic properties over chick embryo neuroepithelial stem cells. *Dev. Biol.* **297**, 402–16 (2006).
24. M. K. Lehtinen, *et al.*, The cerebrospinal fluid provides a proliferative niche for neural progenitor cells. *Neuron* **69**, 893–905 (2011).

25. D. Holland, *et al.*, Structural growth trajectories and rates of change in the first 3 months of infant brain development. *JAMA Neurol.* **71**, 1266–1274 (2014).
26. J. Dubois, *et al.*, The dynamics of cortical folding waves and prematurity-related deviations revealed by spatial and spectral analysis of gyrification. *Neuroimage* **185**, 934–946 (2019).
27. J. West, P. K. Newton, Cellular interactions constrain tumor growth. *Proc. Natl. Acad. Sci. U. S. A.* **116**, 1918–1923 (2019).
28. A. K. Laird, Dynamics of tumour growth: Comparison of growth rates anid extrapolation of growth curve to one cell. *Br. J. Cancer* **19**, 278–291 (1965).
29. H. B. Sarnat, L. Flores-Sarnat, Telencephalic Flexure and Malformations of the Lateral Cerebral (Sylvian) Fissure in *Pediatric Neurology*, (Elsevier Inc., 2016), pp. 23–38.
30. A. Bush, M. Nuñez, A. K. Brisbin, R. M. Friedlander, E. Goldschmidt, Spatial convergence of distant cortical regions during folding explains why arteries do not cross the sylvian fissure. *J. Neurosurg. JNS*, 1–10 (2019).
31. K. E. Garcia, *et al.*, Dynamic patterns of cortical expansion during folding of the preterm human brain. *Proc. Natl. Acad. Sci. U. S. A.* **115**, 3156–3161 (2018).
32. P. M. Thompson, C. Schwartz, R. T. Lin, A. A. Khan, A. W. Toga, Three-dimensional statistical analysis of sulcal variability in the human brain. *J. Neurosci.* **16**, 4261–4274 (1996).
33. S. Caspers, *et al.*, The human inferior parietal cortex: Cytoarchitectonic parcellation and interindividual variability. *Neuroimage* **33**, 430–448 (2006).
34. J. G. Chi, E. C. Dooling, F. H. Gilles, Gyral development of the human brain. *Ann. Neurol.* **1**, 86–93 (1977).
35. C. Clouchoux, *et al.*, Quantitative in vivo MRI measurement of cortical development in the fetus. *Brain Struct. Funct.* **217**, 127–139 (2012).
36. P. A. Habas, *et al.*, Early folding patterns and asymmetries of the normal human brain detected from in utero MRI. *Cereb. Cortex* **22**, 13–25 (2012).
37. R. Wright, *et al.*, Automatic quantification of normal cortical folding patterns from fetal brain MRI. *Neuroimage* **91**, 21–32 (2014).
38. F. Leroy, *et al.*, New human-specific brain landmark: The depth asymmetry of superior temporal sulcus. *Proc. Natl. Acad. Sci. U. S. A.* **112**, 1208–1213 (2015).
39. C. A. Walsh, Genetic malformations of the human cerebral cortex. *Neuron* **23**, 19–29 (1999).
40. G. Lohmann, D. Y. Von Cramon, A. C. F. Colchester, Deep sulcal landmarks provide an organizing framework for human cortical folding. *Cereb. Cortex* **18**, 1415–1420 (2008).
41. C. de Juan Romero, C. Bruder, U. Tomasello, J. M. Sanz-Anquela, V. Borrell, Discrete domains of gene expression in germinal layers distinguish the development of gyrencephaly. *EMBO J.* **34**, 1859–1874 (2015).
42. G. E. Elsen, *et al.*, The protomap is propagated to cortical plate neurons through an Eomes-dependent intermediate map. *Proc. Natl. Acad. Sci. U. S. A.* **110**, 4081–4086 (2013).
43. I. S. Gousias, *et al.*, Magnetic resonance imaging of the newborn brain: manual segmentation of labelled atlases in term-born and preterm infants. *Neuroimage* **62**, 1499–509 (2012).
44. I. S. Gousias, *et al.*, Magnetic Resonance Imaging of the Newborn Brain: Automatic Segmentation of Brain Images into 50 Anatomical Regions. *PLoS One* **8** (2013).
45. N. J. Tustison, B. B. Avants, Explicit B-spline regularization in diffeomorphic image registration. *Front. Neuroinform.* **7**, 39 (2013).
46. B. B. Avants, C. L. Epstein, M. Grossman, J. C. Gee, Symmetric diffeomorphic image registration with cross-correlation: evaluating automated labeling of elderly and neurodegenerative brain. *Med. Image Anal.* **12**, 26–41 (2008).
47. Center for History and New Media, Zotero Quick Start Guide.
48. M. F. Beg, M. I. Miller, A. Trouvé, L. Younes, Computing large deformation metric mappings via

geodesic flows of diffeomorphisms. *Int. J. Comput. Vis.* **61**, 139–157 (2005).

49. A. Gholipour, *et al.*, A normative spatiotemporal MRI atlas of the fetal brain for automatic segmentation and analysis of early brain growth. *Sci. Rep.* **7** (2017).
50. F. Pedregosa, *et al.*, Scikit-learn: Machine Learning in Python. *J. Mach. Learn. Res.* **12**, 2825–2830 (2011).
51. J. Glaister, A. Carass, D. L. Pham, J. A. Butman, J. L. Prince, Automatic falx cerebri and tentorium cerebelli segmentation from Magnetic Resonance Images. *Proc. SPIE--the Int. Soc. Opt. Eng.* **10137** (2017).
52. T. E. Oliphant, Python for scientific computing. *Comput. Sci. Eng.* **9**, 10–20 (2007).
53. P. A. Yushkevich, *et al.*, User-guided 3D active contour segmentation of anatomical structures: significantly improved efficiency and reliability. *Neuroimage* **31**, 1116–28 (2006).

Fig. 1

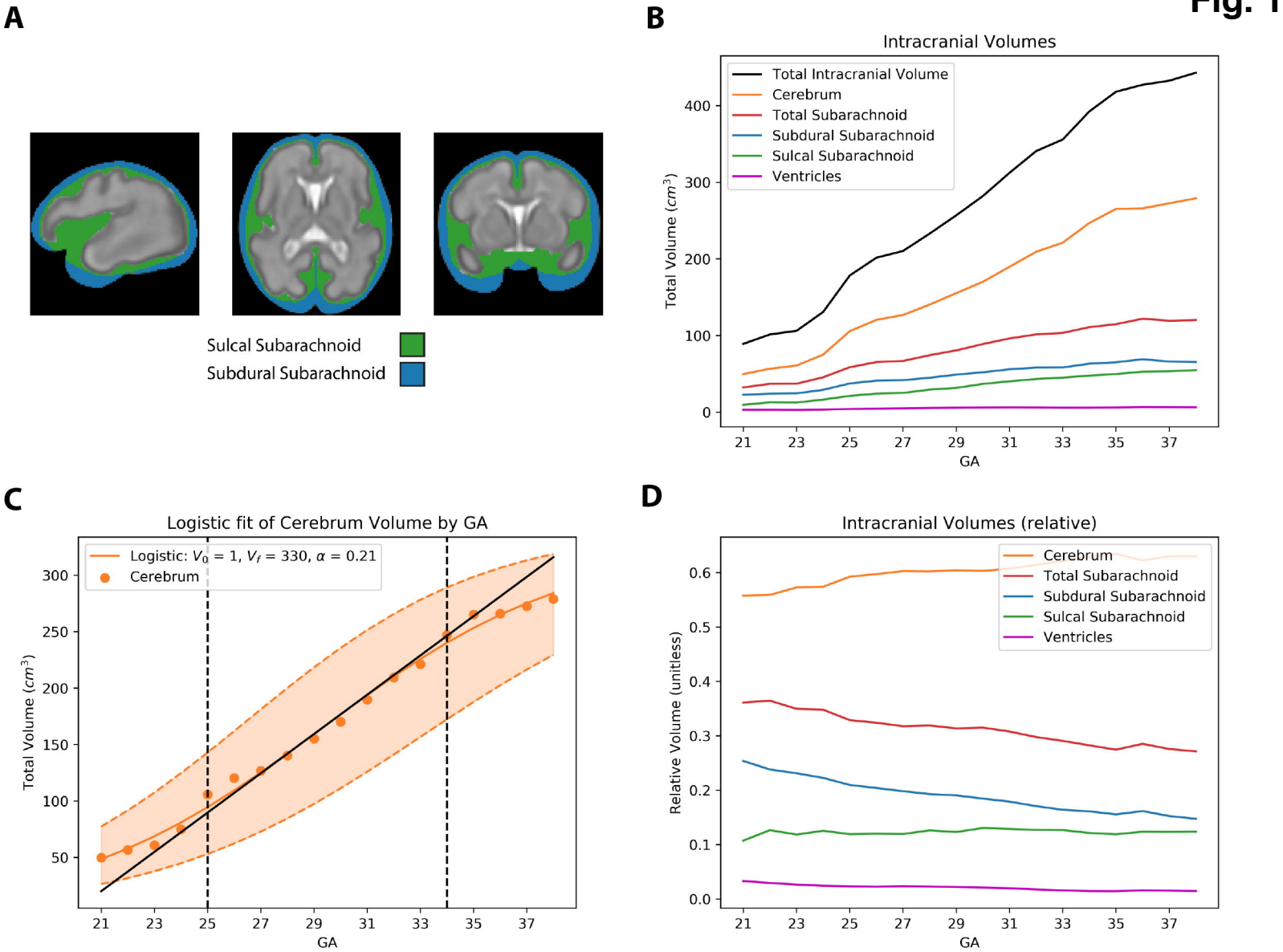
A
Sulcal Subarachnoid
Subdural Subarachnoid
B
Intracranial Volumes
Total Intracranial Volume
Cerebrum
Total Subarachnoid
Subdural Subarachnoid
Sulcal Subarachnoid
Ventricles
Total Volume (cm^3)
GA
C
Logistic fit of Cerebrum Volume by GA
Logistic: V_0 = 1, V_f = 330, α = 0.21
Cerebrum
Total Volume (cm^3)
GA
D
Intracranial Volumes (relative)
Cerebrum
Total Subarachnoid
Subdural Subarachnoid
Sulcal Subarachnoid
Ventricles
Relative Volume (unitless)
GA

Fig. 2

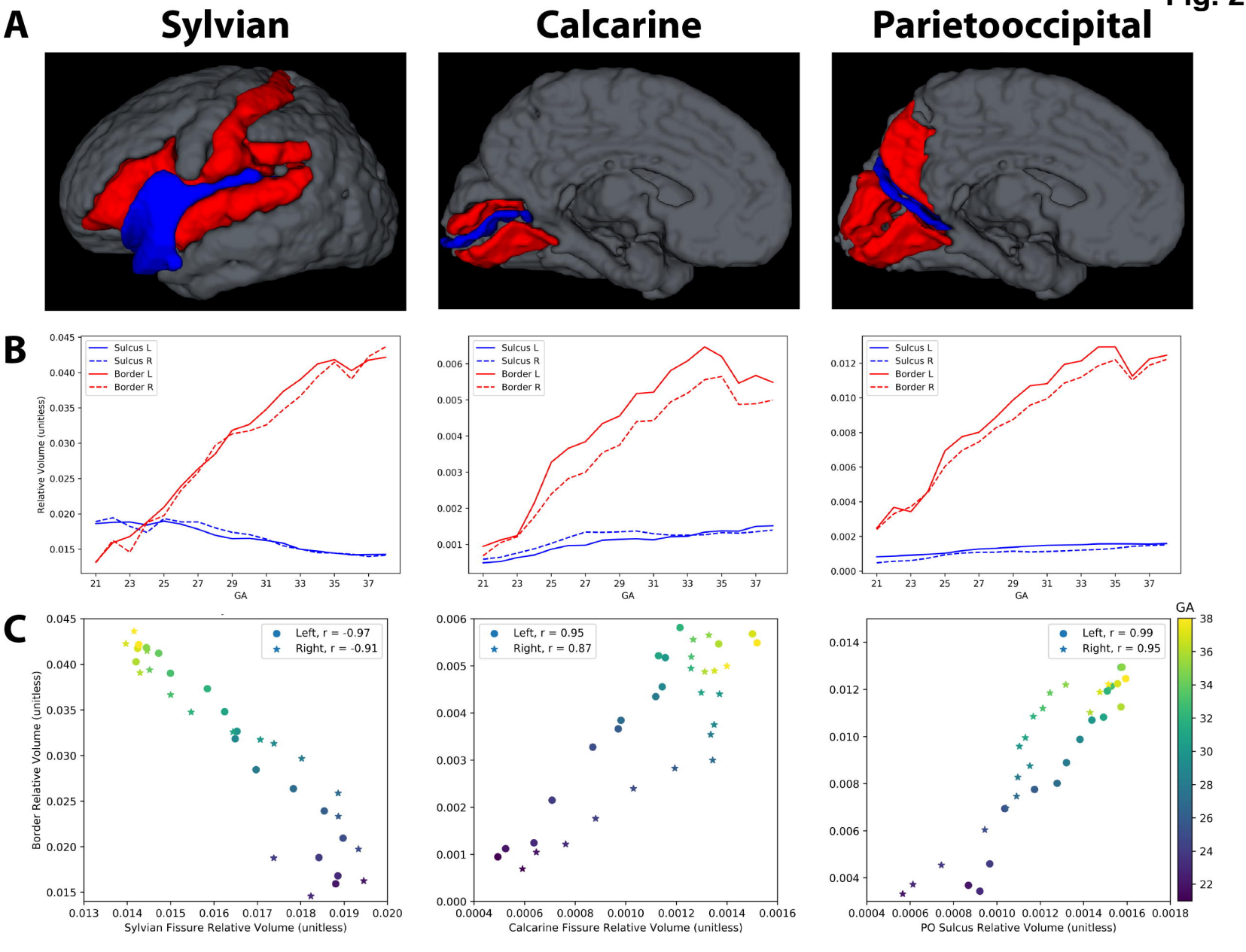
A
Sylvian
Calcarine
Parietooccipital
B
Sulcus L
Sulcus R
Border L
Border R
Relative Volume (unitless)
GA
C
Left, r = -0.97
Right, r = -0.91
Border Relative Volume (unitless)
Sylvian Fissure Relative Volume (unitless)
Left, r = 0.95
Right, r = 0.87
Calcarine Fissure Relative Volume (unitless)
Left, r = 0.99
Right, r = 0.95
PO Sulcus Relative Volume (unitless)
GA

Fig. 3

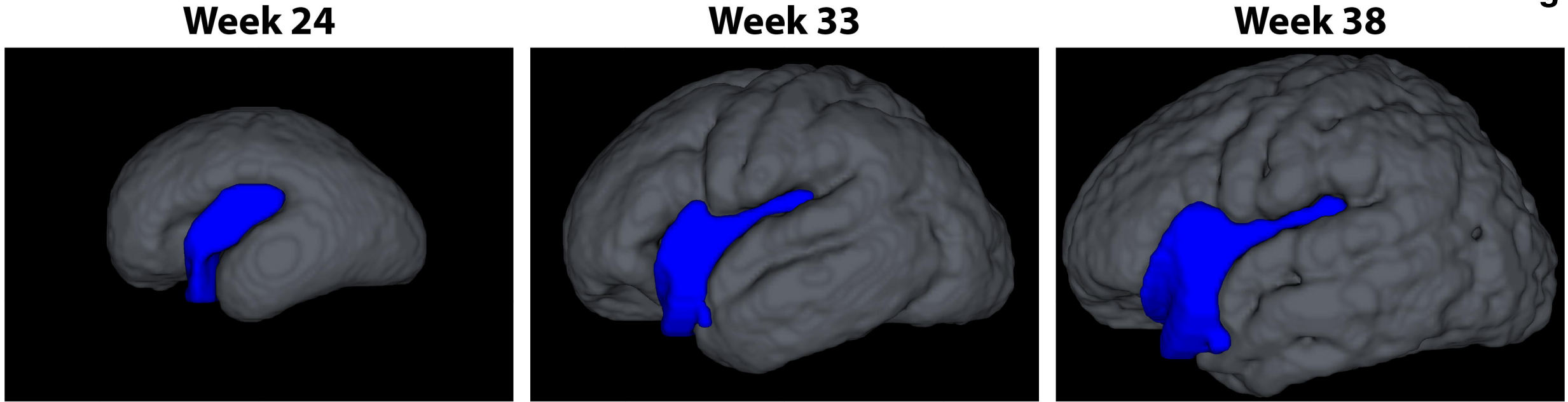

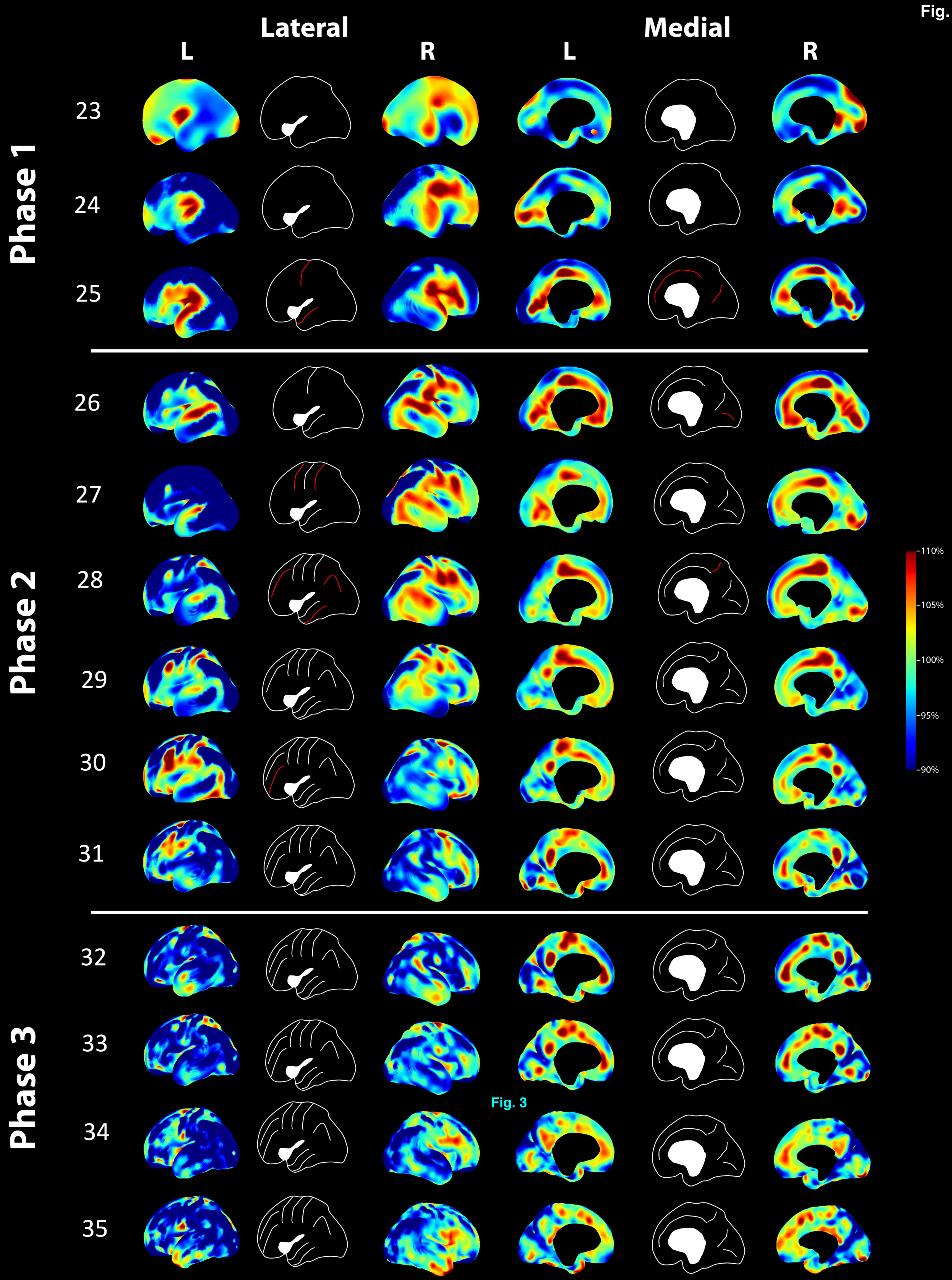
Lateral
Medial
L
R
L
R
Phase 1
23
24
25
Phase 2
26
27
28
29
30
31
Phase 3
32
33
34
35
110%
105%
100%
95%
90%

Fig. 3

Figure 1: Overall growth of cerebrum and constituent tissues. A) Division of subarachnoid space into sulcal (investing sulci) and subdural (superficial to gyri/sulci). The sulcal subarachnoid is a the space within the sulci/fissures of the brain, while the subdural subarachnoid is the CSF between the outer surface of the brain and inner table of the skull. These spaces were divided by a convex hull around each cerebral hemisphere. B) Total intracranial volume by gestational age. The total volume of the cerebrum increased 6-fold, while the subarachnoid space only grew 4-fold and the ventricles 2-fold. C) Logistic fit for cerebral volume growth. Initial predicted volume (V_0) was 1 cm^3, final predicted volume was 330 cm^3, and logistic growth rate (α) was 0.21, corresponding to a maximum weekly growth rate of 17 cm^3 per week at approximately 28 weeks. Dashed orange – 1 S.D. error bars, vertical black dashed lines – periodization of brain growth into 3 phases that correspond to folding patterns (see text). Solid orange – logistic fit. Solid black – linear growth in the second phase of growth. D) Relative intracranial volume by gestational age. Cerebral volume expands from 56% to 63%. Note that while there is relative loss in subarachnoid space, this is largely driven, by loss in subdural subarachnoid (25% to 15%), while sulcal subarachnoid is relatively constant at 11-12%. CSF still constitutes approximately 30% of overall cerebral volume at term.

Figure 2: Sylvian fissure develops differently than other fissures. A) Illustrations of sulci (blue) and bordering gyri (red) at Week 33. B) Relative volume of sulcus compared to that of bordering gyri. For the calcarine and parietooccipital sulci, both sulcus and gyri increase in relative volume, unlike in the Sylvian fissure. C) Correlation between sulcus relative volume and bordering gyri relative volume. The Sylvian fissure ($r = -0.97$) demonstrates a strong negative correlation while the parietooccipital ($r = 0.99$) and calcarine ($r = 0.95$). demonstrate strong positive correlations. The Sylvian fissures shrinks as the opercula grow while the other sulci grow with their bounding gyri.

Figure 3: Sylvian fissure closes over gestation. The Sylvian fissure begins as a flat depression and closes over time through the overgrowth of the opercular gyri. This process is largely complete by Week 33 or earlier. This stands in contrast to the other sulci of the brain and is the prime example of interlobar folding

Figure 4: Jacobian analysis (week-to-week relative volume expansion, correcting for overall volume growth). *Left:* lateral cerebral surface. *Right:* medial cerebral surface. *Rows* – gestational age. The central column in each group demonstrates existing (white) or new (red) sulci at each week.

In phase 1, folding is primarily interlobar with the majority of folding occurring in the perisylvian areas (frontal, parietal, and temporal opercula), forming and closing the Sylvian fissure. In doing so, the major lobes are demarcated In phase 2, folding forms the major named sulci of the brain, proceeding in an orderly fashion from the central sulcus outward. On the medial surface, the parietooccipital and calcarine sulci finish folding and the cingulate sulcus elongates and serves as a source for additional volume expansion. By phase 3 (around GA week 32), the major sulci have completed forming and smaller, non-named sulci are folding. The only area of persistent area growth by week 35 onwards (weeks 36-38 not pictured) is the temporal pole.

Fig. S1

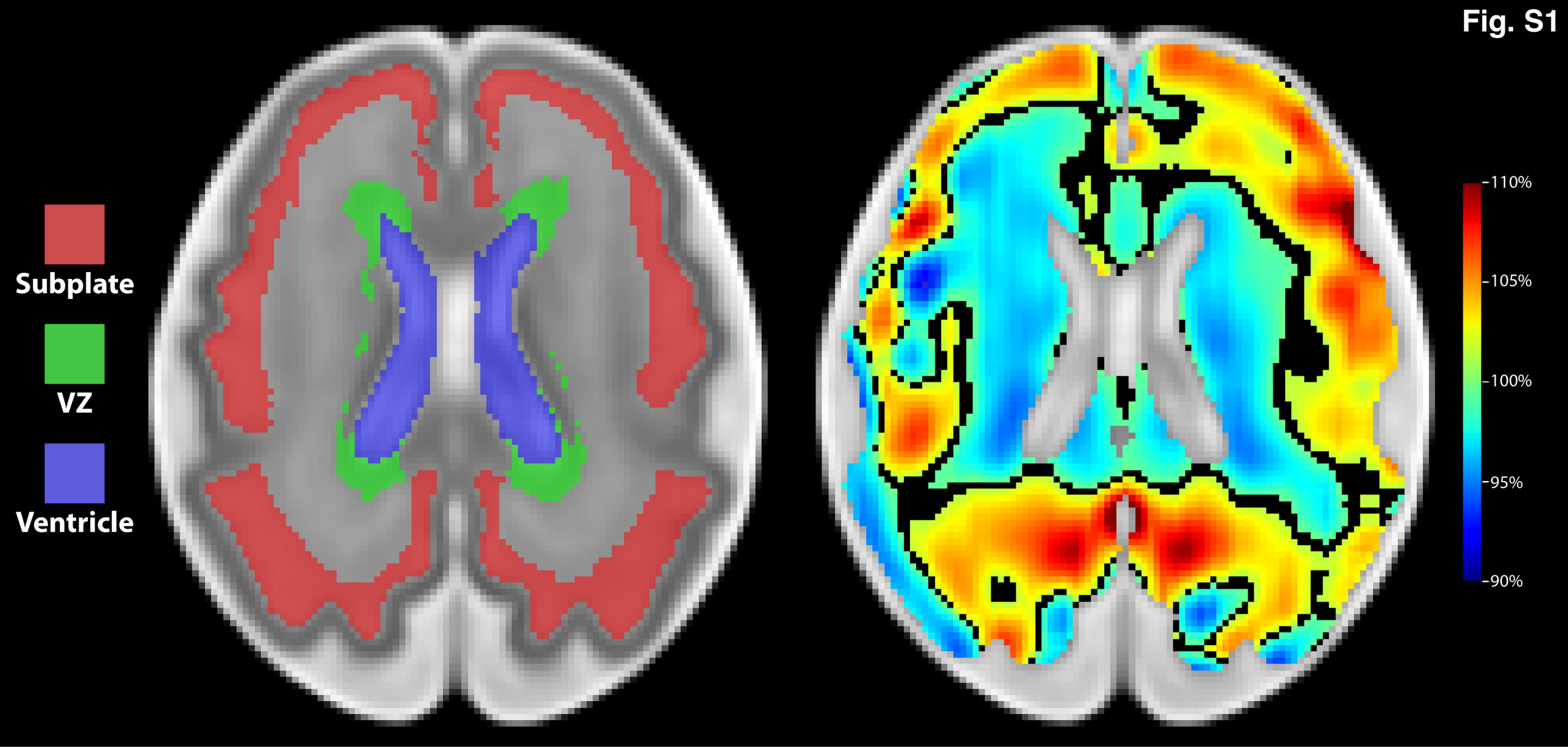

Table S1 – Registration validation: Comparing segmentation overlap (as measured by Dice similarity coefficient) when warped by one week between different registration/warp paradigms

GA	Week 38 to 21	Week 21 to 38	Week 38 to 21 with landmarks
21	0.90	1.00	0.88
22	0.90	0.90	0.89
23	0.91	0.90	0.80
24	0.91	0.90	0.86
25	0.92	0.91	0.90
26	0.93	0.92	0.91
27	0.93	0.93	0.91
28	0.94	0.93	0.91
29	0.93	0.93	0.90
30	0.93	0.93	0.87
31	0.94	0.93	0.89
32	0.94	0.93	0.91
33	0.94	0.94	0.88
34	0.94	0.94	0.88
35	0.89	0.94	0.88
36	0.90	0.89	0.90
37	0.90	0.90	0.89
38	1.00	0.90	1.00

Table S2 – Registration validation: Comparing segmentation overlap (as measured by Dice similarity coefficient) when warped over all weeks between different registration/warp paradigms

GA	Week 38 to 21	Week 21 to 38	Week 38 to 21 with landmarks
21	0.72	1.00	0.56
22	0.72	0.90	0.59
23	0.73	0.88	0.60
24	0.73	0.86	0.63
25	0.74	0.85	0.67
26	0.75	0.83	0.69
27	0.77	0.82	0.71
28	0.78	0.80	0.72
29	0.80	0.78	0.75
30	0.80	0.78	0.77
31	0.82	0.76	0.78
32	0.83	0.75	0.80
33	0.84	0.73	0.81
34	0.86	0.72	0.84
35	0.87	0.71	0.87
36	0.88	0.70	0.88
37	0.90	0.70	0.90
38	1.00	0.68	1.00

Figure S1: Volume expansion is at the cortical plate and subplate. Axial slice for Week 30 at the level of the lateral ventricles. **Left** – segmentations of the subplate, ventricular zone (VZ), and lateral ventricles. **Right** – Jacobian determinant image with scale bar to right. Black lines represent areas of zero nonlinear growth (dividing areas of relative expansion and lack of expansion). Note the area of expansion largely constrained to the cortical and subplate. The ventricular zone is largely quiescent.

Table S1 – Registration validation: Comparing segmentation overlap (as measured by Dice similarity coefficient) when warped by one week between different registration/warp paradigms

We performed three registration paradigms for the nonlinear diffeomorphic registration as described in the text. In the first, using image intensity only (image mutual information), we registered from Week 38 to 37, 37 to 36, and so on ("Week 38 to 21"). Second, also using image intensity only), we registered from Week 21 to 22, 22 to 23, and so on ("Week 21 to 38"). Finally we performed the first registration again (Week 38 to 21) but provided the registration algorithm with landmarks from the preexisting segmentations from the Gholipour et al. atlas ("Week 38 to 21 with landmarks").

Each week had preexisting segmentations from the Gholipour et al. atlas. We used these as the ground truth and compared them to warped segmentation. In Table S1, we warped each segmentation by 1 week using the paradigms described above (i.e Week 38 segmentation warped to Week 37, 37 to 36, etc.) We then computed the overlap of the segmentations using the weighted multiclass Dice similarity.

The first two paradigms that were only intensity-based (Week 38 to 21 and Week 21 to 38) were largely comparable in overlaps, while Week 38 to 21 with landmarks appeared to have slightly poorer registration accuracy. The results in this paper are based off the Week 38 to 21 registration paradigm.

Table S2 – Registration validation: Comparing segmentation overlap (as measured by Dice similarity coefficient) when warped over all weeks between different registration/warp paradigms

We performed three registration paradigms and validated them with the segmentation overlap, as measured by the Dice similarity coefficient. In table S2, we warped the initial segmentation from the atlas (Week 38 for the Week 38 to 21 and Week 38 to 21 with landmarks paradigms, Week 21 for the Week 21 to 38 paradigm) through all weeks. For example, we warped the week 38 segmentation to week 37, then that warped segmentation to week 36, etc. We then computed the overlap of the segmentations using the weighted multiclass Dice similarity.

Lower, though still acceptable, overlap scores were seen the further the initial segmentation was warped, suggesting an accumulation of error. The final accumulated error was slightly lower in the Week 38 to 21 paradigm than the Week 21 to 38 paradigm. Interestingly, the Week

38 to 21 with landmarks paradigm had significantly worse registration accuracy when compared to the intensity-only paradigms, suggesting that providing the preexisting segmentations directly to the registration algorithm worsened its performance. Given these results, we used the Week 38 to 21 paradigm for the remainder of the paper.